# The 30 June 2017 North Sea earthquake: Location, Characteristics, and Context

Annie E. Jerkins[1] (annie@norsar.no)

Hasbi Ash Shiddiqi[2] (Hasbi.Shiddiqi@uib.no)

Tormod Kværna[1] (tormod@norsar.no)

Steven J. Gibbons[1] (steven.gibbons@ngi.no)

Johannes Schweitzer[1,*] (johannes@norsar.no); ORCID: 0000-0002-5986-1492

Lars Ottemöller[2] (Lars.Ottemoller@uib.no)

Hilmar Bungum[1] (Hilmar.Bungum@norsar.no)

[1]NORSAR, [2]University of Bergen, [*] Also at the University of Oslo

## Abstract

The Mw 4.5 southern Viking Graben earthquake on 30 June 2017 was one of the largest seismic events in the Norwegian part of the North Sea the last century. It was well recorded on surrounding broadband seismic stations at regional distances, and it generated high signal-to-noise ratio teleseismic P-arrivals at up to 90 degrees with good azimuthal coverage. Here, the teleseismic signals provide a unique opportunity to constrain the event hypocenter. Depth phases are visible globally and indicate a surface reflection in the P-wave coda some 4 seconds after the initial P-arrival, giving a much better depth constraint than regional S-P time differences provide. Moment tensor inversion results in a reverse thrust faulting mechanism. The fit between synthetic and observed surface-waves at regional distances is improved by including a sedimentary layer. Synthetic teleseismic waveforms

generated based on the moment tensor solution and a near-source 1D velocity model indicate a depth of 7 km. Correlation detectors using the S-wave coda from the main event were run on almost 30 years of continuous multichannel seismic data searching for repeating signals. In addition to a magnitude 1.9 aftershock 33 minutes later, and a few magnitude ~1 events in the following days, a magnitude 2.5 earthquake on 13 November 2016 was the only event found to match the 30 June 2017 event well. Using double-difference techniques, we find that the two largest events are located within 1 km of the main event. We present a Bayesloc probabilistic multiple event location including the 30 June event and all additional seismic events in the region well-recorded on the regional networks. The Bayesloc relocation gave a more consistent seismicity pattern and moved several of the events more towards the west. The results of this study are also discussed within the regional seismotectonic frame-of-reference.

## Introduction

The seismicity of the North Sea is low to intermediate (Bungum et al., 2000; Lindholm and Bungum, 2000; Ottemöller et al., 2005). Most of the earthquakes in the North Sea are located along the Norwegian coastline, in the Viking and Central Grabens, and along the passive margins (Bungum et al., 1991). Usually the seismic events are below magnitude 3. Figure 1 shows the location of the 30 June 2017 event as reported in the Norwegian National Seismic Network (NNSN) bulletin, the main seismicity pattern in the North Sea from 1982 to 2018, as well as available focal mechanisms for events above magnitude 3.5. In the following, we divide the Norwegian part of the North Sea into three different regions: north from 60-62° N, central from 58-60° N and south from 56-58° N. Historically, we know of two larger earthquakes located in the North Sea region: a magnitude 6.1 event on 7 June 1931 in the Dogger Bank area (54.1° N, 1.5° E) and a magnitude 5.2 event off the west coast of Norway (59.8° N, 1.8° E) on 24 January 1927 (Musson, 1994; Bungum et al., 2003). Additionally, on 4 January 1879 a magnitude ($M_L$) 4.8 event occurred in the northern North Sea (61° N, 2° E) (Musson, 2008).

Another moderately sized earthquake (Mw 4.1-4.4) occurred on 7 May 2001 at the Ekofisk oil field in the Central Graben. Ottemöller et al. (2005) concluded that this event was induced by water injection. The depth was determined using spectral and moment tensor analysis, indicating a depth of less than 3 km, which later was confirmed through GPS and differential bathymetry data. Further studies on the moment tensor of the seismic event was conducted by Selby et al. (2005) and Cesca et al. (2011).

The first major overview of earthquake focal mechanisms for areas offshore Norway was published by Bungum et al. (1991), while later studies have been made by Hicks et al. (2000)

and Tjåland and Ottemöller (2018). The northern part of the North Sea is one of the most seismically active regions of Norway, and several focal mechanisms have been calculated for the area (Figure 1). Hicks et al. (2000) found that the focal mechanisms in the region were divided into two groups, reverse to oblique reverse and normal to strike-strip, and generally showed a maximum compressive stress in the WNW-ESE direction. This direction is consistent with a ridge-push force from the Mid-Atlantic ridge as observed also along most of the Norwegian continental margin (Bungum et al., 1991; Fejerskov and Lindholm, 2000; Lindholm et al., 2000). Tjåland and Ottemöller (2018) reviewed previous fault plane solutions and assigned quality measures to these based on the number of polarity observations and the azimuthal coverage. The high-quality solutions agree well with the stress pattern obtained by Hicks et al. (2000).

The focus of this study is an earthquake that occurred on 30 June 2017 at 13.33 UTC with a magnitude of Mw 4.5 in the central part of the North Sea, near the transition between the Viking and Central Grabens. The event was the largest in the area for almost a century, and was reported felt in north-east Scotland, Fair Isle, Orkney, Stavanger in Norway, the Shetland Islands, and on the Sleipner A petroleum platform, with a maximum intensity of 4 (European Macroseismic Scale). No damage related to this earthquake was reported.

The relative lack of seismicity in the central and southern parts of the North Sea, structurally represented by the Viking and Central Grabens, is well known, so in this region we can infer stress directions mostly from borehole *in situ* measurements. However, these measurements are made in boreholes drilled into the sedimentary layers, and may not necessarily represent the stress regime in the underlying basement (Lindholm et al., 1995). Even so, such measurements have shown reasonably consistent compressive stress in the

WNW-ESE direction, in line with the expectation from Mid-Atlantic ridge-push forces (e.g., Richardson et al., 1979; Stein et al., 1989). In the Viking Graben only one focal mechanism has been calculated earlier (oblique normal, 29 July 1982) (Hicks et al., 2000) at a distance of 134 km from the 30 June 2017 event (Figure 1). A new high-quality focal mechanism for the 30 June 2017 earthquake can therefore assist in further inferring a stress direction in the Viking Graben.

The Mesozoic North Sea rift system consists of the Viking Graben (striking largely NS down to $58^{o}$N), the Central Graben (striking southeasterly from $58^{o}$N) and the Moray Firth Graben (striking westwards), coming together at a triple junction (around $58^{o}$N, $1^{o}$E) characterized by a large Middle Jurassic volcanic center. The first stage of the structural evolution of the North Sea region implied initial development of the basin framework during the Early Paleozoic. Subsequently, rifting activity, connected to the Arctic-North Atlantic rift system, continued in the early Triassic, followed by repeated reactivation of existing basement lineaments in response to extensional deformation in the Mesozoic and Cenozoic (Bartholomew et al., 1993). Crustal extension peaked during the Late Jurassic-Early Cretaceous, terminating in the early Eocene when the North Atlantic opened north of the Charlie-Gibbs Fracture Zone (Ziegler, 1992; Talwani and Eldholm, 1977). A model by Bartholomew et al. (1993) invokes the rifting of the North Sea during the Late Jurassic in response to a simple regional stress regime, with a maximum compressive stress direction oriented N-S to NNW-SSE.

This leaves the Viking and Central Grabens essentially as failed rifts during the Early Cenozoic, and there are reasons to assume that the earthquake activity in this region therefore primarily will be expressing the response of existing zones of weakness to the contemporary stress regime (e.g., Lindholm et al., 2000). The seismic activity is relatively high in the northern part of the Viking Graben, slowing down gradually in the southerly direction, and more or less petering out into the Central Graben.

The 30 June 2017 earthquake occurred in the southern Viking Graben and was recorded with high signal-to-noise ratios at stations of the NNSN and British Geological Survey (BGS). In addition, the event was recorded at a large number of global stations. Most seismic events in the North Sea due to their size are recorded only at regional distances. Teleseismic signal onset estimates often have lower traveltime residuals than regional arrivals (e.g. Myers et al., 2015) and this event is a unique opportunity to locate a North Sea earthquake using both regional and teleseismic readings, thereby mitigating possible bias in regional traveltime calculations.

In this study, we estimate a hypocenter location combining regional and teleseismic data, to obtain as accurate an epicenter and depth estimate as possible. We investigate the hypocenter location and the source mechanism. In addition, we have been pursuing potential aftershocks or other similar events on the same fault using correlation detectors. Multiple re-analysis of event locations for clustered seismicity is also used to relocate individual events from the NNSN bulletin.

Since there are several offshore platforms related to oil and gas production in the area, the analysis of this event is important for risk assessment related to production.

## Location in bulletin of the Norwegian National Seismic Network

Instrumentally, the 30 June 2017 earthquake was observed with high signal-to-noise ratios at stations of the NNSN. The NNSN is operated by the University of Bergen in cooperation with NORSAR, where the University of Bergen runs 34 seismic stations covering mainland Norway, Jan Mayen and Svalbard (Ottemöller et al., 2018). NORSAR is responsible for five seismic arrays and four single seismic stations (Schweitzer and Roth, 2015; Gibbons et al., 2019). In addition, we had access to seismic data from the permanent monitoring systems installed on the sea-floor at Ekofisk (operated by Conoco-Phillips), Grane and Oseberg (both operated by Equinor), as well as the stations operated by the British Geological Survey (BGS), the Geological Survey of Denmark and Greenland (GEUS), Swedish Defense Research Agency (FOI) and stations of the Swedish National Seismic Network (SNSN) operated by the University of Uppsala. The detection threshold for seismicity in this region of the North Sea using the NNSN is approximately magnitude 2 (Demuth et al., 2016). Figure 1 shows the earthquake location (green circle) and the stations (red triangles for single stations and red circles for seismic arrays) used to locate the 30 June 2017 earthquake as reported in the NNSN bulletin. The earthquake was well recorded regionally, with a good azimuthal coverage. The NNSN hypocenter parameters and uncertainties are provided in Table 1.

Waveforms from a selected set of stations at different distance and azimuth from the event are shown in Figure 2. The vertical and horizontal components are shown for each station, and the Pn and Sn arrivals are indicated. Generally, the P-phases are picked on vertical components and the S-phases on rotated horizontal components. Accurate S-phase arrival time readings, together with a good velocity model, are necessary for locating low magnitude North Sea events accurately. As a rule of thumb, the depth of local events can be estimated with confidence if there are phase observations at stations located within a distance about twice the event depth (Havskov and Ottemöller, 2010; Havskov et al., 2011). This was not the case for the 30 June 2017 event, as for most regional earthquakes in this area. The closest stations are at the Grane field at a distance of about 50 km (see Figure 1).

To quantify how well the earthquake hypocenter is constrained when using the phase readings from the NNSN bulletin, of which almost all are regional P and S-phases, a 3D grid search was conducted. This is illustrated in Figure 3 (left panel), where a vertical 2D section from the grid search is shown. The grid search was performed using the traveltimes predicted by the NNSN regional velocity model (Havskov and Bungum, 1987) (see right-hand panel of Figure 3). The different colors represent the L1-norm of time residuals. From this vertical section, we observe that the depth resolution between 2 and 17 km is quite limited.

Figure 3 illustrates the depth uncertainty when using only regional P- and S-phase arrival times and we therefore seek additional ways to constrain the depth. As rarely observed in this region, the event was large enough to be recorded teleseismically and accurate depth phase arrival-time measurements may provide tighter constraints (e.g. Heyburn et al., 2013). This will be discussed in the section Depth Estimation using Teleseismic Observations.

## Regional moment tensor inversion

The 2017 earthquake provided clear long-period signals at several regional stations, which enabled us to carry out a moment tensor inversion. In total, we used 22 stations from the Norwegian National Seismic Network (NS), the Great Britain Seismograph Network (GB), the Danish Seismological Network (DK), GEOFON (GE), the Global Seismographic Network (IRIS/USGS) (II/IU), the German Regional Seismic Network (GR) and the Swedish National Seismic Network (UP).

We used the matrix inversion method from Ichinose et al. (2003) (see Data and Resources Section) to obtain the deviatoric moment tensor. The data were bandpass filtered between 0.02 and 0.07 Hz. Green's functions were computed using a fast reflectivity and frequency-wavenumber (f-k) summation technique (Zeng and Anderson, 1995) for hypocentral depths between 1 and 15 km depth with 1 km increment. Different velocity models were tested to identify which 1D model best represents the regional crustal structure (see Table 2): the 1D NNSN model for the Northern North Sea (Havskov and Bungum, 1987), and an averaged Crust1.0 model (Laske et al., 2012) for the North sea and surrounding regions. Additionally, we created another model by adding a sedimentary layer of 2 km to the NNSN model. The thickness of this layer was taken as the average of the Crust1.0 model for the North Sea and the surrounding area (Laske et al., 2012). The velocity models are shown in the electronic supplement. To account for origin time uncertainty from the hypocenter solution, the origin time of the synthetics were for alignment purposes shifted up to ± 3.0 seconds.

Most of the usable regional observations are from stations in Norway and Great Britain, but additional stations from other countries were included to improve the azimuthal coverage. The waveform fits for stations in Northern Germany and the Netherlands were generally poor, which was most likely caused by thick sediments (8-10 km) in these regions (Artemieva and Thybo, 2013). The lower signal to noise ratio was also a problem on their records.

To determine the best result, we calculated the variance reduction (VR) of the inversion results using the following equation:

$$VR = \left(1 - \frac{\sum(observed - synthetic)^2}{\sum observed^2}\right) x\ 100\ \%\ . \qquad (1)$$

As seen from Equation 1, a high VR represents a good fit between observed and synthetic data. The uncertainty of the moment tensor inversion calculation is indirectly represented by the VR. The Crust1.0 model with sedimentary layer (see table available in the electronic supplement) produced the highest VR (see Table 2) with a thrust mechanism for a hypocentral depth of 7 km, as illustrated in Figure 4. Both fault planes are striking NNW-SSE. The corresponding axis of maximum compressive stress is nearly horizontal with an azimuth of 80° while the axis of minimum compressive stress is near vertical with a trend of 324°. A comparison of observed and synthetic waveforms is shown in the electronic supplement. Our moment tensor inversion result is slightly different to the GCMT results (Table 3 and Figure 4c), with the GCMT solution giving slightly larger strike-slip contributions, a greater depth and a larger Mw.

For the NNSN and Crust1.0 models, the use of a sedimentary layer increased the respective variance reductions. The significant improvement caused by the addition of a sedimentary layer to the velocity models can be seen on the surface waves at the transverse components especially at epicentral distances > 500 km (see Figure 5). At these distances the amplitude of surface waves becomes dominant and larger than the body waves. The cross-correlation coefficients between observed and synthetic data are increased. As for the stations that have a close epicentral distance, which are mostly located in Norway (Network code NS), the cross-correlation coefficients are also slightly increased. However, it seems that the inclusion of sedimentary layer does not significantly improve the waveform modelling for these stations.

## Depth Estimation using Teleseismic Observations

The event of 30 June 2017 was relatively large for the North Sea region, and numerous teleseismic observations are available at all azimuths. Figure 6 displays stations at both regional and teleseismic distances for which body-wave arrivals were picked to locate the event. Separate symbols on the map indicate stations with first P-arrivals only, with both P- and S-arrivals, and with clear depth phase observations. The azimuthal coverage of all observations is good, and notably so also for the depth phases. Several studies show that reliable measurements of (pP/sP – P) traveltime differences can often offer the best depth constraints (e.g. Engdahl et al., 1998; Ottemöller et al., 2009). Heyburn et al. (2013) investigated how the global observability of depth phases was likely to vary with focal mechanism and demonstrated that dip-slip mechanisms (as observed here) are expected to excite strong pP depth phases at teleseismic distances and at a wide range of azimuths.

The event was located with the HYPOSAT algorithm (Schweitzer, 2001; Schweitzer, 2018) (see Data and Resources Section) using the regional and teleseismic observations from the stations shown in Figure 6. HYPOSAT uses information such as first onsets and later arrivals, plus additional information from ray parameters, azimuths and arrival time differences to calculate the best fitting hypocenter of a seismic source using generalized matrix inversion (Schweitzer, 2001). For calculation of more accurate pP and sP traveltimes, the HYPOSAT algorithm was extended to accommodate the use of a different 1D local velocity model for the source region, combined with global models.

The local 1D-velocity model used better describes the source region and includes a sedimentary layer in the upper part of the model. The model is shown in Figure 3b. Here it is assumed that the geological conditions of the nearest hydrocarbon field (the Gudrun field) are similar to those of the source region. The distance between the source region and the Gudrun field is approximately 10 km. The upper 5 km of the local 1D model is based on averaging the sedimentary velocities obtained from a well-log in the northern part of the Gudrun field (velocities from the well-log is shown by the thin black line in Figure 3b). The sedimentary layers were extended down to 8 km using a gradual increase in sedimentary velocities. Below 8 km we assume crustal velocities similar to those of the Fennoscandian 1D velocity model (FESCAN) (Mykkeltveit & Ringdal, 1981).

In addition to using the 1D local velocity model for the source region, two global models were included in the location: FESCAN and ak135 (Kennett et al., 1995). Further, a second location was evaluated using all the same criteria and just interchanging the FESCAN model with the NNSN model (see velocity models in Figure 3b).

The local velocity model was used at distances up to 1°, FESCAN/NNSN between 1 and 14° and ak135 beyond 14°. The local velocity model was used between 0-1° since it better describes the crustal structures of the immediate source region than regional models. For distances between 1 and 14° the FESCAN/NNSN models better represents the crustal and upper mantle structures of this region than the globally averaged ak135 model. The crustal thickness of the NNSN model is 31 km, which is representative for the North Sea and western Norway regions. The FESCAN model has a crustal thickness of 40 km, and better represents the thicker crust in the continental regions of Fennoscandia.

A total of 341 phases (P, S, PcP and pP) from 246 stations with an azimuthal gap of 27° were used as input to the HYPOSAT algorithm. The estimated locations are provided in Table 4 and the corresponding 95% uncertainty estimates in Table 5. The event depth is determined to be between 6 and 7 km. Overall, the FESCAN model gave lower residuals than the NNSN model. This was particularly pronounced for stations at far-regional distances above 10°, where the station residuals indicate that the FESCAN model better represents the crustal and upper mantle structures along the regional propagation paths. Consequently, the hypocenter associated with the FESCAN model is considered here to be the preferred location.

The vertical component of the observed seismograms from the stations shown with black symbols in the map of Figure 6 are presented in Figure 7a. The waveforms are sorted by azimuth and filtered in the 1-3 Hz band. For the array stations, standard beamforming procedures were performed to improve the signal-to-noise ratio. The vertical arrows indicate the first P-phase and the depth phase. The time-aligned traces show a relatively consistent time difference of 4.25 seconds between the two phases at all stations, supporting the depth phase hypothesis.

The signal from CMAR (Chiang Mai array, Thailand), approximately 78° from the epicenter, holds clear P and depth phase arrivals, and is shown as the red seismogram in Figure 7a. In order to further constrain the event depth and verify the presence of a depth phase in the signal, synthetic seismograms were estimated for the CMAR array using the *hudson96* program (Herrmann, 2013) (see Data and Resources Section). This program uses the theoretical inversion approach developed by Hudson (1969).

Synthetic seismograms were calculated for source depths between 1 and 12 km in steps of 1 km, using the ak135 model and the GCMT focal mechanism for modelling wave propagation to teleseismic distances. However, a 1D velocity model with sedimentary layers (see local model of Figure 3b) was used in *hudson96* for modelling wave propagation in the source region. The GCMT mechanism was used since it gave a better fit between the observed and synthetic teleseismic seismograms than the mechanism obtained from the regional surface wave data in this study. The exact reason for this observation is not fully understood. However, due to the source process and lateral heterogeneities in the source region, the short period radiation pattern of a seismic event does not have to be equal to the longer period radiation pattern, which is dominating moment tensor solutions. In our case it appears teleseismically observed short period radiation pattern is in better correspondence with the GCMT solution than with the moment tensor solution estimated from regional data.

The modelling results are presented in Figure 7b (filtered between 1.5 and 3.5 Hz). The observed and synthetic seismograms show the largest similarity for a source at a depth between 6 and 7 km, indicated by the red-colored seismograms. The synthetic seismogram shows a clear depth phase arrival, where the first P arrives 4.25 seconds prior to the depth phase. This is consistent with what is observed in the seismograms recorded at CMAR. Using an estimated depth of 6.5 km, waveform modelling was performed for the remaining stations of Figure 7a. The results are presented in Figure 8, where a) shows unfiltered synthetic seismograms, b) synthetic seismograms filtered between 1.5 and 3.5 Hz, and c) observed seismograms filtered between 1 and 3 Hz. In order to ensure similar dominant signal frequencies, the synthetic seismograms were filtered at slightly higher frequencies than the observed data. Comparing the seismograms in Figure 8b and 8c, both the synthetic and observed data show aligned traces with a relatively consistent time difference of 4.25 seconds between the two phases at all stations, which again supports the earlier depth phase hypothesis and the associated hypocentral depth.

The unfiltered synthetic seismograms of Figure 8a show a clear depth phase arrival at all stations having a reversed polarity as compared with the first-arriving P. This is a strong indication of the depth phase being pP as pP leaves the source in the compressional quadrant upward, while P leaves downward from the same quadrant. About 1-2 seconds later, another weak phase arrival can be seen in the modelled waveforms (indicated by an arrow in Figure 8b), which corresponds with the travel time of sP. The sP arrival is most clearly seen on the modelled waveforms at stations with azimuths between 159-244°. For this GCMT focal mechanism (reverse fault) it is known that pP is radiated with larger amplitudes than the sP (see e.g., Heyburn, 2013).

## Aftershocks and Related Seismicity

In the North Sea and along the Norwegian continental margin there is a great variety in aftershock occurrence, with end members represented by the 8 August 1988 Mw 5.3 Møre Basin earthquake, with no previous observed seismicity in the epicentral region and no observed aftershocks (Hansen et al., 1989), and two events offshore western Norway in 1986 (Mw 4.7) and 1989 (Mw 5.2), both with a number of observed aftershocks (Bungum and Alsaker, 1991). Given Båth's Law, and even more so the fact that the largest aftershock from the 1986 and 1989 events was between 2 and 3 $M_L$ units smaller than the main event, this indicates that in most cases for this low seismicity region possible aftershocks will simply not be detected. However, the tool now provided by the multi-channel correlation detector of Gibbons and Ringdal (2006) has changed this, giving us a chance to go much lower in magnitude in search for both previous and subsequent activity on or nearby the causative fault.

For example, by using a $M_L$ 3.5 earthquake from a costal site in Northern Norway as a full waveform template, repeating seismicity from the same region could be monitored down to $M_L$ 0.5 using the NORSAR array at a distance of 550 km (Gibbons et al., 2007). This array station is at a similar distance to the North Sea earthquake and we can attempt a similar procedure. The NORSAR array has two advantages in monitoring for low-magnitude seismic events close to a well-recorded master event at regional distances using correlation detector. The first one is the large number of sensors and their considerable separation, resulting in a template with a high time-bandwidth-product and providing a low background level for the detection statistic. The second advantage is the long archive of continuous waveform data. A template covering the Sn-arrival and coda was extracted for the 30 June 2017 event and correlated against continuous data starting in December 1995 using a bandpass filter between 2 and 5 Hz. This date corresponds to the time of the upgrade of the seismometers and digitizers, and the increase of the sampling rate from 20 to 40 Hz. In almost 23 years of correlation of the waveform archive with the signal template, only four significant triggers were registered. Three small aftershocks were detected in the 48 hours following the main event. The largest, with magnitude 1.9, occurred 32 minutes after the main event. A single event of magnitude 2.4 on November 13, 2016, is the only occasion in this time-span on which a similar signal was recorded prior to June 2017. The signals generated by the smallest aftershocks are well below the noise level and we display the waveforms for all these correlation triggers as recorded at the KMY station (Figure 9).

To further investigate the location of the triggered events, we analyzed data from six stations at different directions from the main event. If the triggered signals at these stations correlate with the correct time delays with the signal template of the main event, we can conclude that the triggered events are co-located with the main event.

We see in Figure 10 that the S-wave templates from the main shock correlate well with signals from the two largest events at six different stations, surrounding the source as displayed. Each correlation trace displays a local peak, which is at a significantly higher level than at surrounding samples. Minimizing the time-differences over a geographic grid (details of the procedure provided in Gibbons et al., 2017) demonstrate that both the 13 November 2016 earthquake and the largest aftershock on 30 June 2017 were located in the immediate vicinity of the main shock. Given the anticipated rupture length associated with the main shock of approximately 1 km, and the spatial resolution of a few hundred meters indicated for these S-wave double difference calculations (see Figure 10c and 10d), we can assume that the relative locations of these events are essentially co-located. The small differences indicated in Figure 10c and 10d are within the region of uncertainty of several hundred meters. A relative location was not attempted for the two smallest events displayed in Figure 9 since a satisfactory correlation was not possible on stations surrounding the source.

Multiple re-analysis of event locations for clustered seismicity can improve location estimates for individual events significantly (e.g. Myers et al., 2007; Nooshiri et al., 2017). The Bayesloc Bayesian hierarchical probabilistic multiple event location algorithm (see Data and Resources Section) calculates joint probability distributions for event hypocenters, phase identification labels, phase reading uncertainties and, most significantly, corrections to seismic traveltime predictions. The traveltime prediction corrections are estimated from large numbers of events, many of which are well constrained. The corrections mitigate inaccuracies in the velocity model applied and reduce the location bias for those events with relatively few observations. With its many global and regional recordings, and additional depth constraints, the June 30 earthquake is such an event which can be assigned very tight priors in the Bayesloc location. The presence of this event increases the quality of the time-correction probability distributions for the region and improve location estimates for nearby events.

Figure 11 displays the output from the Bayesloc program (red symbols) for a number of the better observed events in the Central North Sea. The NNSN catalog has been supplemented with additional readings from other stations, including the large aperture NORSAR array and numerous temporary deployments. A more clustered image of seismicity emerges in the relocated events than in the single-event location estimates (yellow symbols) and it appears that many of the largest earthquakes in the period 2000-2018 occur significantly further to the west. The oil fields are included together with the earthquake locations in Figure 11 to show the importance of locating natural seismic events in the North Sea. Many of the largest relocation vectors in Figure 11 are found to be associated with apparent timing or phase pick errors on one or more stations. Uncorrected timing anomalies with significant influence on the single-event location estimates have demonstrably reduced influence on the multiple event location distributions. The ability of Bayesloc to improve the traveltime predictions for all arrivals increases the relative size of the traveltime residuals for the few readings subject to timing errors and makes it easier for them to be ignored in the final location estimates.

## Discussion and Conclusions

The 30 June 2017 Viking Graben earthquake was well recorded at both regional and teleseismic distances and we could exploit teleseismic depth phases to provide constraints on the focal depth. The introduction of a local 1D model with low velocity sedimentary layers was necessary to convert the observed pP-P differential times into a more accurate depth estimate. The inclusion of the local model gave an event depth of 6-7 km. This depth is supported by synthetic modelling of seismograms and from the calculation of the moment tensor. The event most likely occurred in the Baltica basement which is found at a depth of 6 to 9 km in the South Viking Graben (Fazlikhani et al., 2017).

For earthquake locations, the uncertainties related to the event depth are normally considerably higher than for the epicenter location (Engdahl et al., 1998; Havskov and Ottemöller, 2010). Here these uncertainties are significantly reduced through the inclusion of depth phases and a local velocity model with a sedimentary layer. As seen from Figure 3a, phases from the regional network provided little resolution on the focal depth estimate. It was also shown that including a sedimentary layer in the estimation of the moment tensor reduced the variance significantly.

The epicenter reported in the regional NNSN seismic bulletin had a latitude uncertainty of 2.5 km and a longitude uncertainty of 4.2 km. The uncertainties from the HYPOSAT location algorithm are represented by 95% uncertainty ellipses (see Table 4). The major and minor half axes of the ellipses varied between 2.3 and 1.2 km. It should be noted that the calculated uncertainties include reading uncertainties and uncertainties related to station geometry, and other factors such as systematic errors are not included. The distribution of the locations obtained using the HYPOSAT-algorithm (which included both regional and teleseismic phases) as well as the location provided in the NNSN bulletin (which included only regional phases) provide a more realistic picture of the location uncertainties. The epicenter locations in Table 4 are separated by about 4 km. Both of these locations used the same input data except for the regional velocity model, showing the importance of the model. The epicenter of the NNSN bulletin is located in-between the HYPOSAT locations given in Table 4.

The origin time uncertainties provided in Table 1 and Table 5 are computed using different methods, and are therefore not directly comparable. For more information, we refer to the manuals of the programs used for estimation: Ottemöller et al. (2019) and Schweitzer (2018).

All the epicenter estimates lie between 8-10 km from the Gudrun oil/gas field. Examining a relationship between production and earthquakes is of importance in the North Sea. Addressing this question requires additional data from the source region and for the 2017 event is not the main focus of this work. However, we present some of the background. The Gudrun field was discovered in 1975 and is a high temperature high pressure field that started producing in 2014.

Numerous studies have been conducted globally indicating the importance of induced seismicity (e.g., Simpson et al., 1988; Dahm et al., 2007; Ellsworth, 2013; Foulger et al., 2018). Causes of reservoir induced earthquakes can be both related to injection and extraction of fluids (Dahm et al., 2007; Ellsworth, 2013). As of 2017, extraction at Gudrun has been carried out without fluid injection. The focal mechanism could potentially indicate if the derived stress direction deviates from the regional pattern (e.g. Dahm et al., 2007; Ellsworth, 2013). The mechanism here is reverse, which is expected and agrees with the regional stress pattern. While most induced earthquakes occur close to the production sites, there are examples of events being induced/triggered several kilometers away, due changes in the stress field caused by the hydrocarbon production (Ellsworth, 2013; Foulger et al., 2018). An $M_w$ 4.5 earthquake in a stable continental region has a rupture length in the order of 1 km (Wells and Coppersmith, 1994; Leonard, 2010), which combined with the location uncertainty, makes it difficult to associate with any particular mapped structure (Figure 11). The event in terms of mechanism and size is not unexpected for this region. Currently, we have no evidence that the earthquake is triggered by stress changes due to hydrocarbon production. However, this could potentially be addressed in future studies and would require more data from the nearby hydrocarbon fields.

We advocate the application of multiple-event location methods to build up a more accurate picture of the spatial distribution of seismicity. Probabilistic and deterministic methods which can compensate for shortcomings in seismic traveltime predictions can sharpen the image and help to identify mislocated events and possible instrumental timing errors, which may contribute to poor catalog location estimates. We perform a Bayesloc relocation of some of the larger events in the North Sea over the past two decades and find far more clustered seismicity than is observed in the single-event catalog locations. Many earthquakes are relocated further to the west (See Figure 11).

The largest previously recorded earthquake in the North Sea was on 23 January 1989 and had a moment magnitude of 5.2. Most of the earthquake mechanisms in this region reflect thrust to oblique thrust faulting and with a compressional axis in the NW-SE direction, consistent with ridge-push forces (Bungum et al., 1991; Lindholm et al., 2000; Hicks et al., 2000).

The North Sea earthquake focal mechanism obtained in this study is largely consistent with these observations and with stress modelling results (Gölke et al., 1996; Fejerskov and Lindholm, 2000) which indicate a NW-SE to WNW-ESE compressive stress field in Europe with 10-20 MPa averaged over a 100 km thick lithosphere (Gölke and Coblenz, 1996). A compressional direction of $80^{o}$ for the present earthquake is a slight deviation from the main trend, but certainly within the expected range of scatter. There are two main reasons for such deviations, firstly that the stress axes are assumed to bisect the angles between the nodal planes, while we know that this angle for thrust mechanisms is more often around $30^{o}$ than $45^{o}$ (e.g. Sibson, 1985). Secondly, the stress field at any particular place is the superposition of tectonic stress and more regional and local sources of stress such as effects of rebound and glacial load cycles, structural features, erosion and sedimentation, and lateral inhomogeneities in general. Such features have been modelled (Gölke and Coblentz, 1996; Fejerskov and Lindholm, 2000), but not (to our knowledge) the effects of the crustal thinning in the Viking Graben, which in general should contribute to a stress concentration. For smaller to moderate size earthquakes, local variations are expected to influence the stress direction and can therefore give some deviation from the main trend.

This study has added to our understanding of the regional seismotectonics in the southern Viking Graben, including the stress orientation, which is generally consistent with the ridge-push force from the Mid-Atlantic seafloor spreading. Additionally, it was shown that including a local velocity model with lower velocities for the shallower layers resulted in an improved correspondence between observed and modelled depth phases and an improved determination of the event depth, which always is a challenge for an earthquake so far from any shoreline.

## Acknowledgements

We would like to thank the Norwegian National Seismic Network (NNSN) project in which this research was carried out. The financial support to the NNSN project is given by the Norwegian Oil and Gas Association.

We would also like to express our gratitude to Equinor for providing well-log information from the Gudrun field and data from ocean-bottom installations at Grane and Oseberg, and to Conoco-Phillips for providing ocean-bottom data from the Ekofisk field.

It should be noted that the results and interpretations expressed in this paper are those of the authors only.

Finally, we would like to express our gratitude to the editors and reviewers who contributed with comments and feedback.

## Data and Resources

Waveform data were obtained from the Norwegian National Seismic Network, the Incorporated Research Institutions for Seismology (IRIS), and the Observatories and Research Facilities for European Seismology (ORFEUS) European Integrated Data Archive (EIDA). Some of the figures were created using the Generic Mapping Tools (www.soest.hawaii.edu/gmt, last accessed December 2018; Wessel et al., 2013). The moment tensor inversion was conducted using Moment Tensor Inversion Toolkit (MTIV) (Ichinose et al., 2014) (http://crack.seismo.unr.edu/htdocs/students/Ichinose/, last accessed February 2019).

The software described in Herrmann et al. (2013) was obtained from http://www.eas.slu.edu/eqc/eqc_cps/TUTORIAL/ (last accessed February 2019).

The Bayesloc multiple event location software and documentation was obtained from https://www-gs.llnl.gov/nuclear-threat-reduction/nuclear-explosion-monitoring/bayesloc (last accessed February 2019).

Coordinates of the boundaries of the production fields and the faults in the North Sea were obtained from the Norwegian Petroleum Directorate's website on http://www.npd.no/en/Maps/Fact-maps/ (last accessed February 2019), and the oil fields from the British sector was obtained from the British Oil and Gas Authority, website https://data-ogauthority.opendata.arcgis.com/ (last accessed February 2019).

The HYPOSAT algorithm and its manual by Schweitzer (2018) are obtained from http://www.gfz-potsdam.de/bib/pub/nmsop/hyposat.6_0c.zip (last accessed January 2019)

The moment tensor from the Global centroid moment tensor catalogue by (Ekström et al., 2012) was obtained from https://www.globalcmt.org/CMTsearch.html (last accessed January 2019).

An electronic supplement addressing the more detailed aspects of the moment tensor inversion is available. This electronic supplement contains figures that show the velocity models used in the moment tensor inversion, and waveform fits of the best moment tensor result. The table of the best velocity model (averaged Crust1.0 1D model) is also included in this supplement.

## References


Artemieva, I.M., and H. Thybo (2013). EUNAseis: A seismic model for Moho and crustal structure in Europe, Greenland, and the North Atlantic region, *Tectonophysics* **609** 97-153.

Bartholomew, I.D., J.M. Peters and C.M. Powell (1993). Regional structural evolution of the North Sea: oblique slip and the reactivation of basement lineaments, *Petroleum Geology Conference series (Geological Society, London)* **4** 1109-1122.

Bungum, H., A. Alsaker, L.B. Kvamme and R.A. Hansen (1991). Seismicity and seismotectonics of Norway and surrounding continental shelf areas, *J. Geophys. Res*. **96** 2249-2265.

Bungum, H. and A. Alsaker (1991). Source spectral inversion for two earthquake sequences offshore western Norway, *Bull. Seismol. Soc. Am*. **81** 358-378.

Bungum, H., C.D. Lindholm, A. Dahle, G. Woo, F. Nadim, J.K. Holme, O.T. Gudmestad, T. Hagberg and K. Karthigeyan (2000). New seismic zoning maps for Norway, the North Sea and the U.K., *Seismol. Res. Lett*. **71(6)** 687-697.

Bungum, H., C.D. Lindholm and A. Dahle (2003). Long period ground motions for large European earthquakes, 1905-1992, and comparisons with stochastic predictions, *Journal of Seismology* **7** 377-396.

Cesca, S.T. Dahm, C. Juretzek and D. Kühn (2011). Rupture process of the 2001 May 7 Mw 4.3 Ekofisk induced earthquake, *Geophys. J. Int.* **187** 407-41.

Dahm, T., F. Krüger, K. Stammler, K. Klinge, R. Kind, K. Wylegalla, and J.R. Grasso (2007). The 2004 Mw 4.4 Rotenburg, northern Germany, earthquake and its possible relationship with gas recovery, *Bull. Seismol. Soc. Am.* **97(3)** 691–704.

Demuth, A., L. Ottemöller and H. Keers (2016). Ambient noise levels and detection threshold in Norway, *Journal of Seismology* **20** 889-904.

Ekström, G., M. Nettles and A.M. Dziewonski (2012). The global CMT project 2004-2010: Centroid-moment tensors for 13,017 earthquakes. *Phys. Earth. Planet. In.* **200-201** 1-9.

Engdahl, E.R., R. van der Hilst and R. Buland (1998). Global Teleseismic Earthquake Relocation with Improved Travel Times and Procedures for Depth Determination, *Bull. Seismol. Soc. Am*. **88(3)** 722-743.

Ellsworth, W.L. (2013). Injection-induced earthquakes, *Science* **341(6142)** 1225942.

Fazlikhani, H., H. Fossen, R.L. Gawthorpe, J.I. Faleide, and R.E. Bell (2017). Basement structure and its influence on the structural configuration of the northern North Sea rift, *Tectonics* **36(6)** 1151–1177.

Fejerskov, M. and C. Lindholm (2000). Crustal stress in and around Norway: an evaluation of stress-generating mechanisms, *Geological Society, London, Special Publications* **167** 451-467.

Foulger, G.R., M.P. Wilson, J.G. Gluyas, B.R. Julian and R.J. Davies (2018). Earth-Science Reviews Global review of human-induced earthquakes, *Earth-Science Rev.* **178** 438–514.

Gibbons, S.J. and F. Ringdal (2006). The detection of low magnitude seismic events using array-based waveform correlation, *Geophys. J. Int.* **165** 149-166.

Gibbons, S.J, M.B. Sørensen, D. Harris and F. Ringdal (2007). The detection and location of low magnitude earthquakes in northern Norway using multi-channel waveform correlation at regional distances, *Phys. Earth Planet. In.* **160** 285-309.

Gibbons, S.J., F. Pabian, S.P. Näsholm, T. Kværna and S. Mykkeltveit (2017). Accurate relative location estimates for the North Korean nuclear tests using empirical slowness corrections, *Geophys. J. Int.* **208** 101-117.

Gibbons, S.J., J. Schweitzer, T. Kværna and M. Roth (2019). Enhanced detection and estimation of regional S-phases using the 3-component ARCES array, *Journal of Seismology* **23(2)** 341-355.

Gölke, M., S. Cloething and D. Coblentz (1996). Finite-element modelling of stress patterns along the Mid-Norwegian continental margin, $62^{o}$ to $68^{o}$N, *Tectonophysics* **266** 33-53.

Gölke, M. and D. Coblentz (1996). Origins of the European regional stress field, *Tectonophysics* **266** 11-24.

Hansen, R.A., H. Bungum and A. Alsaker (1989): Three recent larger earthquakes offshore Norway, *Terra Nova* **1** 284-295.

Havskov, J., and H. Bungum (1987). Source parameters for earthquakes in the northern North Sea, *Norsk Geologisk Tidsskrift* **67** 51–58.

Havskov, J. and L. Ottemöller (2010). *Routine Data Processing in Earthquake Seismology*, Springer, New York.

Havskov, J., P. Bormann and J. Schweitzer (2011). Seismic source location. In: Bormann, P. (Ed.), *New Manual of Seismological Observatory and Practice 2 (NMSOP-2).*

Herrmann, R.B. (2013). Computer programs in seismology: An Evolving Tool for Instruction and Research, *Seismol. Res. Lett*. **84 (6)** 1081-1088.

Heyburn, R., N.D. Selby and B. Fox (2013). Estimating earthquake source depths by combining surface wave amplitude spectra and teleseismic depth phase observations, *Geophys. J. Int*. **194** 1000-1010.

Hicks, E.C., C.D. Lindholm and H. Bungum (2000). Stress inversion of focal mechanism solutions from onshore and offshore Norway, *Norsk Geologisk Tidsskrift* **80** 235-250.

Hudson, J.A. (1969). A quantitative evaluation of seismic signals at teleseismic distances – II. Body waves and surface waves from an extended source, Geophys. J. Roy. Astr. Soc. 18 353-370.

Ichinose, G.A., J.G. Anderson, K.D. Smith and Y. Zeng (2003). Source parameters of eastern California and western Nevada earthquakes from regional moment tensor inversion, *Bull. Seismol. Soc. Am*. **93(1)** 61-84.

Ichinose, G.A., J. Roman-Nieves and G. Kraft (2014). Moment tensor inversion toolkit (MTINV) version 3.0.3 (http://crackseismo.unr.edu/htdocs/students/Ichinose).

Kennett, B.L.N. , E.R. Engdahl and R. Buland (1995). Constraints on seismic velocities in the Earth from traveltimes, *Geophys. J. Int.* **122(1)** 108–124.

Laske, G., G. Masters, Z. Ma and M.E. Pasyanos (2012). CRUST1.0: An Updated Global Model of Earth's Crust. In: *Geophysical Research Abstracts EGU General Assembly-* 2011, 3743.

Leonard, M. (2010). Earthquake Fault Scaling: Self-Consistent Relating of Rupture Length, Width, Average Displacement, and Moment Release, *Bull. Seismol. Soc. Am*. **100(5A)** 1971–1988.

Lindholm, C.D, H. Bungum, R.K Bratli, B.S. Aadnøy, N. Dahl, B. Tørudbakken and K. Atakan (1995). Crustal Stress in the northern North Sea as inferred from borehole breakouts and earthquake focal mechanisms, Terra Nova **7(1)** 51-59.

Lindholm, C.D. and H. Bungum (2000). Probabilistic seismic hazard; A review of the seismological frame of reference with examples from Norway, *Soil Dyn. Earth. Eng*. **20** 27-38.

Lindholm, C.D., H. Bungum, E. Hicks and M. Villagran (2000). Crustal stress and tectonics in Norwegian regions determined from earthquake focal mechanisms, *Geol. Soc. London Spec. Publ.* **167(1)** 429-439.

Musson, R.M.W. (1994). A Catalogue of British Earthquakes, British Geol. Surv. Technical Rept. WL/94/04.

Musson, R.M.W (2008). The Case for Large M > 7 Earthquakes Felt in the UK in Historical Times, in: Historical Seismology - Interdisciplinary Studies of Past and Recent Earthquakes, J. Fréchet, M. Meghraoui and M. Stucchi (Ed.), Springer, 187-207.

Myers, S.C., N.A. Simmons, G. Johannesson and E. Matzel (2015). Improved Regional and Teleseismic P-Wave Travel-Time Prediction and Event Location Using a Global 3D Velocity Model, *Bull. Seismol. Soc. Am.* **105** 1642-1660.

Myers, S.C., G. Johannesson and W. Hanley (2007). A Bayesian hierarchical method for multiple-event seismic location, *Geophys. J. Int*. **171** 1049-1063.

Mykkeltveit, S. and F. Ringdal (1981). Phase identification and event location at regional distances using small aperture array data. In: *Identification of seismic sources – Earthquake or underground explosions*, Reidel Publishing Company, 467–481.

Nooshiri, N., Saul, J., Heimann, S., Tilmann, F., and Dahm, T. (2017). Revision of earthquake hypocentre locations in global data sets using source-specific station terms, *Geophys. J. Int.* **208** 589-602.

Ottemöller, L., H.H. Nielsen, K. Atakan, J. Braunmiller and J. Havskov (2005). The 7 May 2001 induced seismic event in the Ekofisk oil field, North Sea, *J. Geophys. Res.* **110** B10301.

Ottemöller, L., B. Baptie and N.J.P. Smith (2009). Source Parameters for the 28 April 2007 Mw 4.0 Earthquake in Folkstone, United Kingdom, *Bull. Seismol. Soc. Am.* **99(3)** 1853–1867.

Ottemöller, L., M.L. Strømme and B.M. Storheim (2018). Seismic monitoring and data processing at the Norwegian National Seismic Network, in Summary of the Bulletin of the International Seismological Centre 2015 January-June.

Ottemöller, L., P. Voss and J. Havskov (2019). Seisan earthquake analysis software. Downloaded from: http://seisan.info (21.11.2019).

Richardson, R., S.C. Solomon and N.H. Sleep (1979). Tectonic stress in the plates, *Rev. Geophys. Space Phys*. **17** 981-1019.

Schweitzer, J. (2001). HYPOSAT – An enhanced routine to locate seismic events, *Pure. Appl. Geophys.* **158** 277-289.

Schweitzer, J and M. Roth (2015). The NORSAR Data Center (FDSN Network Code NO). Biannual Report prepared for the FDSN Meeting during IUGG General Assembly in Prague, 2015. Downloaded from: https://www.fdsn.org/media/meetings/2015/NORSAR_Network_Report.pdf

(06.05.2019).

Schweitzer, J. (2018). User manual for HYPOSAT 6 and HYPOMOD 2. In: *New Manual of Seismological Observatory and Practice 2 (NMSOP-2),* P. Bormann (Ed.).

Selby, N., E. Eshun, H.J. Patton and A. Douglas (2005). Unusual long-period Rayleigh wave radiation from a vertical dip-slip source: The 7 May 2001 North Sea Earthquake, *J. Geophys. Res.* **110** B10304.

Sibson, R.H. (1985). A note on fault reactivation. *J. Struct. Geol*. **7** 751-754.

Simpson, D.W, W.S. Leith and C.H. Scholz (1988). Two Types of Reservoir-Induced Seismicity, *Bull. Seismol. Soc. Am* **78(6)** 2025-2040.

Stein, S., S. Cloetingh, N.H. Sleep, and R. Wortel (1989). Passive margin earthquakes, stresses and rheology, in: *Earthquakes at North Atlantic Passive Margins: Neotectonics and Postglacial Rebound*, S. Gregersen and P. W. Basham (Ed.), Kluwer Academic, Dordrecht, 231-259.

Talwani, M. and O. Eldholm (1977). Evolution of the Norwegian-Greenland Sea, *Bull. Seismol. Soc. Am.* **88** 969-999.

Tjåland, N. and L. Ottemöller (2018). Evaluation of seismicity in the area between the Troll field and the Øygarden Fault. Project report. Department of Earth Science, University of Bergen.

Wessel, P., W.H.F. Smith, R. Scharroo, J. Luis, and F. Wobbe (2013). Generic mapping tools: improved version released, *EOS Trans AGU* 94.

Wells, D. L. and K. J. Coppersmith (1994). New empirical relationships among magnitude, rupture length, rupture width, rupture area, and surface displacement. *Bull.*

*Seismol. Soc. Am.* **84** 974-1002.

Zeng, Y.H., and J.G. Anderson (1995). A Method for Direct Computation of the Differential Seismogram with Respect to the Velocity Change in a Layered Elastic Solid, *Bull. Seismol. Soc. Am.* **85(1)** 300–307.

Ziegler, P.A. (1992). North Sea rift system, P.A. Ziegler (Ed.) in: Geodynamics of Rifting Case History Studies on Rifts: Europe and Asia, *Tectonophysics* **208** 55-75.

## Full mailing address and affiliation for each author


Annie E. Jerkins[1] (annie@norsar.no)

Hasbi Ash Shiddiqi[2] (Hasbi.Shiddiqi@uib.no)

Tormod Kværna[1] (tormod@norsar.no)

Steven J. Gibbons[1] (steven.gibbons@ngi.no)

Johannes Schweitzer[1,*] (johannes@norsar.no); ORCID: 0000-0002-5986-1492

Lars Ottemöller[2] (Lars.Ottemoller@uib.no)

Hilmar Bungum[1] (Hilmar.Bungum@norsar.no)

[1]NORSAR: NORSAR, Gunnar Randers Vei 15, 2007 Kjeller, Norway

[2]University of Bergen: Department of Earth Science, Allégaten 41, 5007 Bergen, Norway

[*] Also at the University of Oslo: The Centre for Earth Evolution and Dynamics (CEED), P.O Box 1028 Blindern, 0315 Oslo, Norway

## Tables

***Table 1: Event location from the Norwegian National Seismic Network (NNSN) seismic bulletin. The abbreviation NSTA is the number of stations used for the location.***

| NNSN | Origin date/time | Latitude | Longitude | Depth | NSTA | RMS | ML |
|---|---|---|---|---|---|---|---|
| Results | 2017 06 30<br>13:33:46.3 | 58.98°N | 1.79°E | 11.0 km | 108 | 0.7 | 4.2 |
| Uncertainty | 1.95 s | 2.5 km | 4.2 km | 3.0 km | | | 0.2 |

***Table 2: List of velocity models used in the moment tensor inversion and the variance reductions for each model.***

| No. | Velocity Model | Variance reduction (%) |
|---|---|---|
| 1 | NNSN model | 47.1 |
| 2 | NNSN model + sedimentary layer from Crust1.0 | 60.3 |
| 3 | Crust1.0 without sedimentary layer | 54.0 |
| 4 | Crust1.0 with sedimentary layer | 68.4 |

***Table 3: Comparison between the moment tensor solution in this study and the GCMT.***

| Solution | Focal Mechanism (Strike/Dip/Rake) | Depth (km) | Mo (Nm) | Mw | DC % |
|---|---|---|---|---|---|

| | | | | | |
|---|---|---|---|---|---|
| This study | 161/42/78<br>358/50/101 | 7 | 6.7 x $10^{15}$ | 4.5 | 73.6 % |
| GCMT | 146/57/57<br>17/45/130 | 12 | 1.73 x $10^{16}$ | 4.8 | 69.5 % |

***Table 4: Locations estimates using HYPOSAT with regional and teleseismic phases, including depth phases.***

| MODEL | Origin time | Latitude | Longitude | Depth | NSTA |
|---|---|---|---|---|---|
| Local sediment + NNSN + AK135 | 2017 06 30 13:33:45.5 | 58.98°N | 1.75°E | 6.3 km | 246 |
| Local sediment + FESCAN + AK135 | 2017 06 30 13:33:44.6 | 58.96°N | 1.81°E | 7.0 km | 246 |

***Table 5: 95% uncertainty estimates for the locations found in Table 4.***

| **MODEL** | **Uncertainty ellipse major half axis** | **Uncertainty ellipse minor half axis** | **Azimuth of ellipse major axis** | **Depth uncertainty** | **Origin time uncertainty** |
|---|---|---|---|---|---|
| Local sediment + NNSN + AK135 | 2.3 km | 1.9 km | 124.8° | 0.7 km | 0.13 s |
| Local sediment + FESCAN + AK135 | 1.4 km | 1.2 km | 155.0° | 0.6 km | 0.09 s |

## List of Figure Captions

*Figure 1: Seismotectonic overview of the North Sea. The red triangles (single stations) and circles (array stations) show the seismic stations with phase readings used in the NNSN location of the 30 June 2017 event. The grey symbols show events as far back as 1982 for which waveforms were available, and where phases were repicked and then jointly relocated*

*as part of this study. The events thus represent the main seismicity pattern since 1982. The event symbols are scaled according to the magnitude of the events. Available focal mechanisms for events larger than magnitude 3.5 are shown and are, for display purposes, scaled up by a factor of two relative to the other event symbols (grey). Additionally, the focal mechanism from the study on the Ekofisk event by Cesca et al. (2011) is included. The location and focal mechanism of the June 2017 events are shown by the green symbols. The Viking Graben (VG) and Central Graben (CG) are indicated on the map. More detailed information on the North Sea rift structures and faults are provided in Figure 11.*

*Figure 2: Unfiltered waveforms on selected regional stations at different distances and azimuths from the 30 June 2017 event. The event to station distances and azimuths are given on the right-hand side of the panel. The stations KMY (Karmøy) and SKAR (Skarslia) are located in Norway, LRW (Lerwick) on the Shetland Islands and EKB (Eskdalemuir) in Scotland. The locations of the North Sea stations Grane and Ekofisk stations are shown in the map of Figure 1.*

*Figure 3: a) L1-norm time residuals from grid search using NNSN readings and the NNSN velocity model. The 2D grid is centered on the estimated longitude of the event as provided in the NNSN bulletin (1.79°E), and the latitude and depth axes are plotted to an equivalent kilometer scale. The red star indicates the latitude and depth of the NNSN location estimate. b) The solid red line shows the NNSN P-wave crustal velocity model, whereas the solid black line represents the P-wave crustal velocity model of the FESCAN model (Mykkeltveit & Ringdal, 1981). The blue line shows a representative crustal model with sedimentary layers*

*for the source region, while the thin black line (below the blue line) represents the P-wave velocities from a well-log north in the Gudrun field, approximately 8-10 km away from the NNSN earthquake location estimate.*

*Figure 4: Focal mechanism solution obtained from this study along with the stations (red triangles) used in the inversion. (b) The plot of source depth vs variance reduction percentage, each of the focal mechanisms is labeled with the magnitude (Mw). The best focal mechanism is shown by the black arrow. (c) Comparison between the focal mechanism obtained in this study and the focal mechanism provided by the GCMT. The strike, dip, rake and moment magnitude for these focal mechanisms are available in Table 3.*

*Figure 5: Example of waveform fit comparison between the moment tensor results using Crust1.0 (a) without sediment, and (b) with sediment. The displacement observed waveforms (black lines) and synthetic waveforms (red lines) are plotted for three components (Z: vertical, R: Radial, and T: Transverse components). The station and network codes are written on the top of each trace along with hypocentral distances (R), azimuth (Az), and time shift for each station (ts). The unit of the traces are in [µm]. On the upper left of each trace, the individual trace time shift and the cross-correlation coefficient are shown respectively.*

*Figure 6: Observations from the 30 June 2017 event. The blue dots mark selected stations with P-phase readings, and red dots mark stations with both P- and S-readings. Black*

*symbols indicate seismic arrays (circles) and 3-component stations (triangles) with particularly clear depth phases. The dashed circle marks 15° of the epicenter (white square).*

*Figure 7: a) Observations of P and depth phases from the 30 June 2017 event at teleseismic distances, sorted by azimuth. The locations of the different stations shown in this panel are shown by black symbols in Figure 6. The vertical arrows indicate the first P-phase and the depth phase. The time-aligned traces show a relatively consistent time difference of 4.25 seconds between the two phases at all stations. The signal from CMAR (Chiang Mai array, Thailand) holds clear P and depth phase arrivals, and is shown as the red seismogram. The data is filtered between 1.5 and 3.5 Hz. b) Waveform modelling at CMAR at different source depths. The best fit between the observed and synthetic data was at 6-7 km, indicated by the red seismograms. The data is filtered between 1 and 3 Hz.*

*Figure 8: a) Waveform modelling at teleseismic stations using a source at 6.5 km depth (unfiltered). b) Waveform modelling of at teleseismic stations using a source at 6.5 km depth (filtered 1-3 Hz). c) Observations at teleseismic distance (filtered 1.5-3.5 Hz). All the modelling is performed using the hudson96 algorithm.*

*Figure 9: Seismic events found by waveform correlation to be related to the 30 June 2017 event recorded on the NNSN station KMY at a distance of 200 km from the epicenter. All events were found using a 42-channel correlation detector on the NORSAR-array (distance*

*550 km) using the S-wave train from the main event as a signal template. The waveforms are filtered in a 2-5 Hz frequency band.*

*Figure 10: Location relative to the 30 June 2017 main event (Event 2017-06-30 13:33:45) for the 13 November 2016 earthquake (panel c) and the largest aftershock on 30 June 2017 (panel d). All relative time-delay measurements were made using templates covering the S-wave arrival and coda. Panel (a) shows the correlation detection statistic traces for two events on the stations indicated in the map (b). The double-difference time-residual grids are displayed for the two events in panels (c) and (d).*

*Figure 11: Selected events from the NNSN bulletin in the period 2000-2018 (yellow symbols) and their relocations using the Bayesloc probabilistic multiple event location algorithm (red symbols). The major faults of the North Sea area are shown with grey lines and the major structures of the Mesozoic rift system are shown with black lines. Bayesloc generates joint probability distributions both for event hypocenters and for correction terms for travel time predictions. The largest relocation vectors (the longest lines) can in most cases be associated with timing errors on one or more stations. The clear green regions indicate the extent of North Sea production fields as indicated by the Norwegian Petroleum Directorate, while the lighter green regions are the production fields as given by the British Oil and Gas Authority. The location of the 30 June 2017 event is shown by the blue symbol.*

## Figures

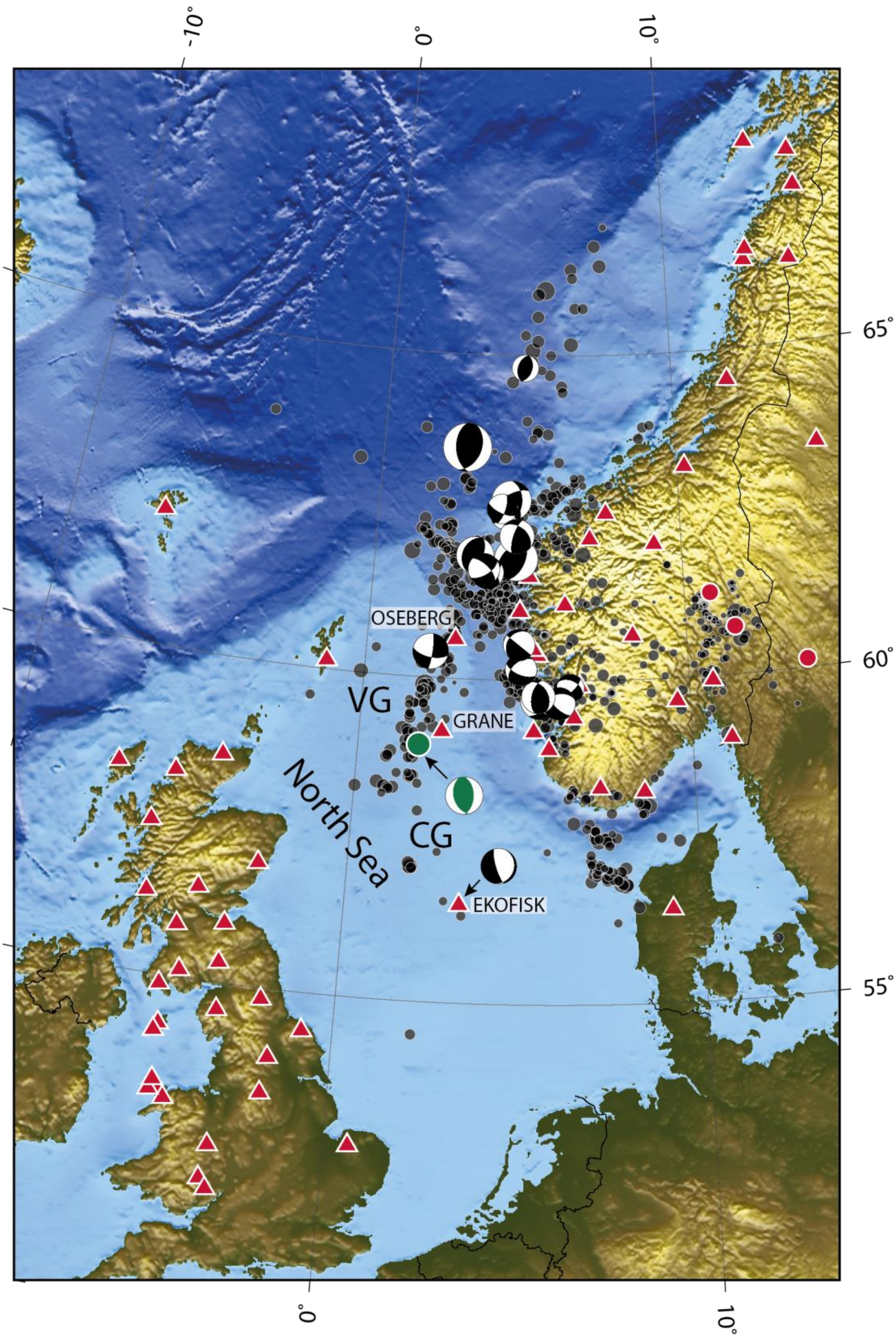


*Figure 1: Seismotectonic overview of the North Sea. The red triangles (single stations) and circles (array stations) show the seismic stations with phase readings used in the NNSN*

*location of the 30 June 2017 event. The grey symbols show events as far back as 1982 for which waveforms were available, and where phases were repicked and then jointly relocated as part of this study. The events thus represent the main seismicity pattern since 1982. The event symbols are scaled according to the magnitude of the events. Available focal mechanisms for events larger than magnitude 3.5 are shown and are, for display purposes, scaled up by a factor of two relative to the other event symbols (grey). Additionally, the focal mechanism from the study on the Ekofisk event by Cesca et al. (2011) is included. The location and focal mechanism of the June 2017 events are shown by the green symbols. The Viking Graben (VG) and Central Graben (CG) are indicated on the map. More detailed information on the North Sea rift structures and faults are provided in Figure 11.*

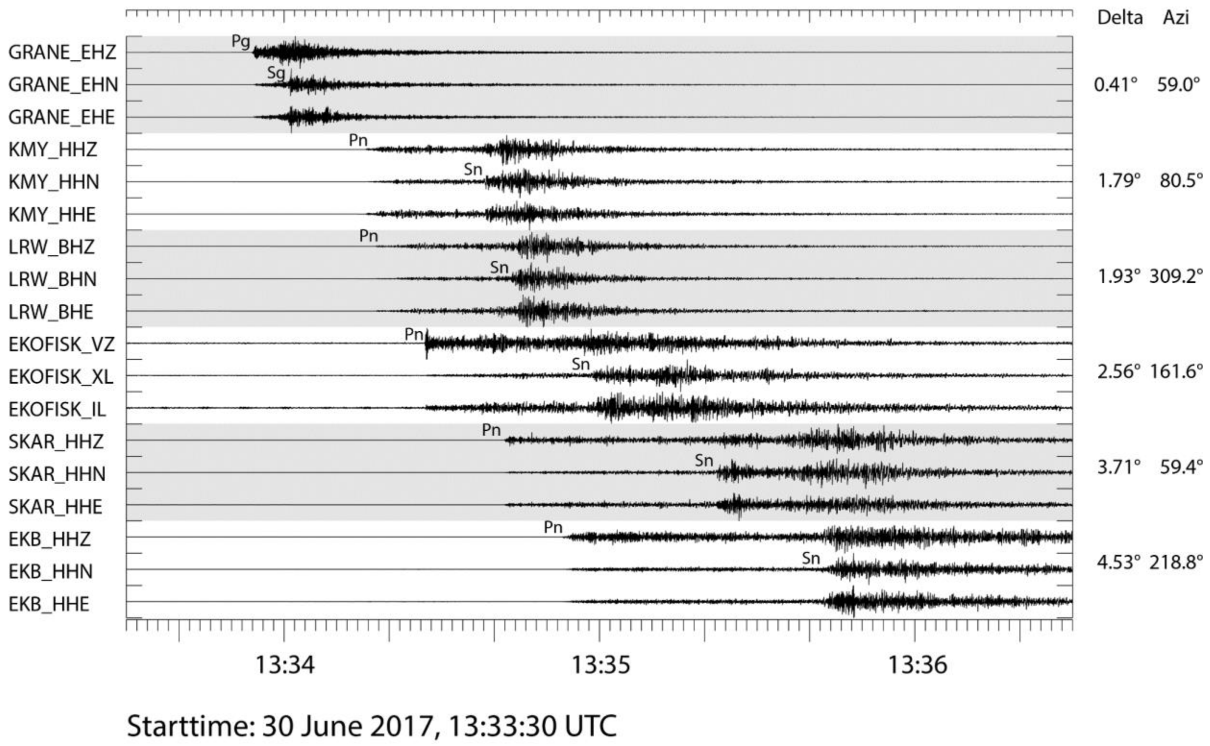


*Figure 2: Unfiltered waveforms on selected regional stations at different distances and azimuths from the 30 June 2017 event. The event to station distances and azimuths are given on the right-hand side of the panel. The stations KMY (Karmøy) and SKAR (Skarslia) are*

located in Norway, LRW (Lerwick) on the Shetland Islands and EKB (Eskdalemuir) in Scotland. The locations of the North Sea stations Grane and Ekofisk stations are shown in the map of Figure 1.

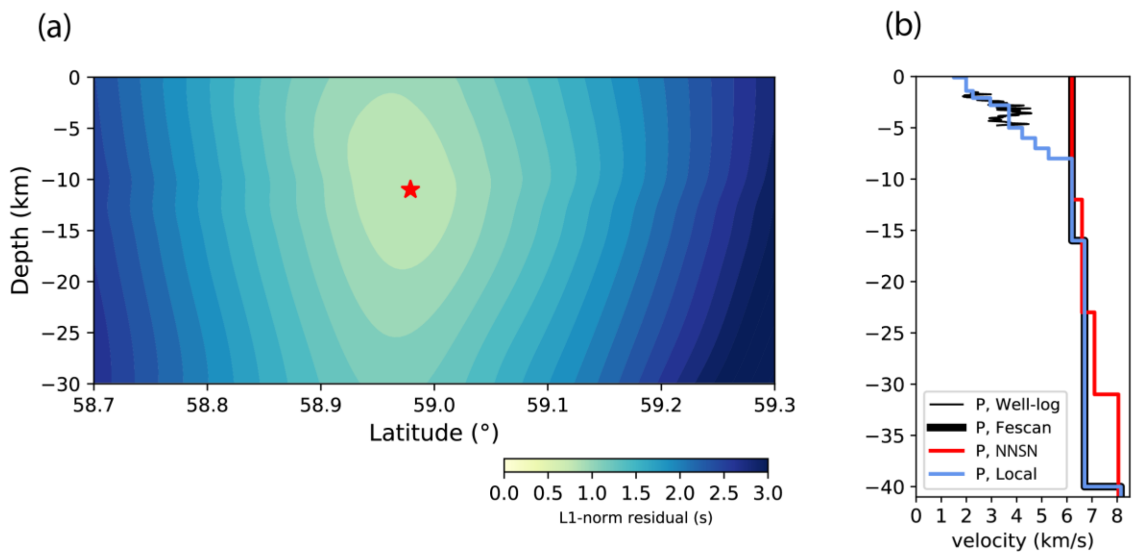


*Figure 3: a) L1-norm time residuals from grid search using NNSN readings and the NNSN velocity model. The 2D grid is centered on the estimated longitude of the event as provided in the NNSN bulletin (1.79°E), and the latitude and depth axes are plotted to an equivalent kilometer scale. The red star indicates the latitude and depth of the NNSN location estimate. b) The solid red line shows the NNSN P-wave crustal velocity model, whereas the solid black line represents the P-wave crustal velocity model of the FESCAN model (Mykkeltveit & Ringdal, 1981). The blue line shows a representative crustal model with sedimentary layers for the source region, while the thin black line (below the blue line) represents the P-wave velocities from a well-log north in the Gudrun field, approximately 8-10 km away from the NNSN earthquake location estimate.*

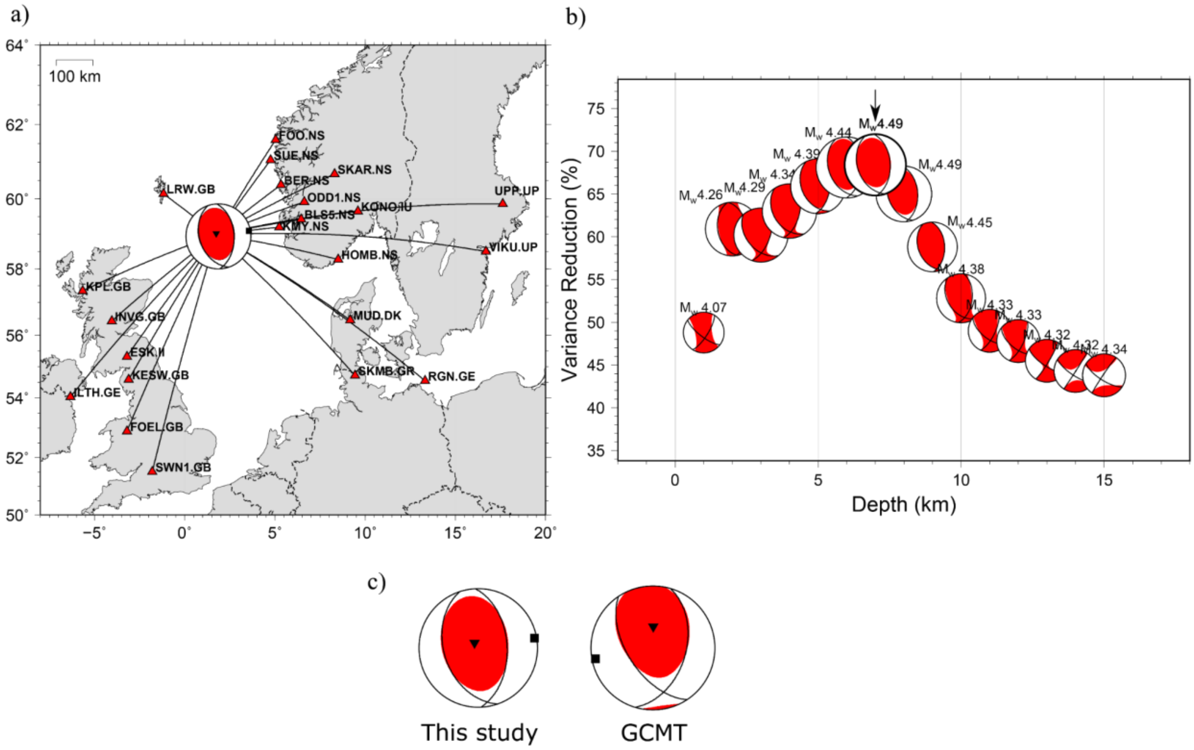


*Figure 4: Focal mechanism solution obtained from this study along with the stations (red triangles) used in the inversion. (b) The plot of source depth vs variance reduction percentage, each of the focal mechanisms is labeled with the magnitude (Mw). The best focal mechanism is shown by the black arrow. (c) Comparison between the focal mechanism obtained in this study and the focal mechanism provided by the GCMT. The strike, dip, rake and moment magnitude for these focal mechanisms are available in Table 3.*

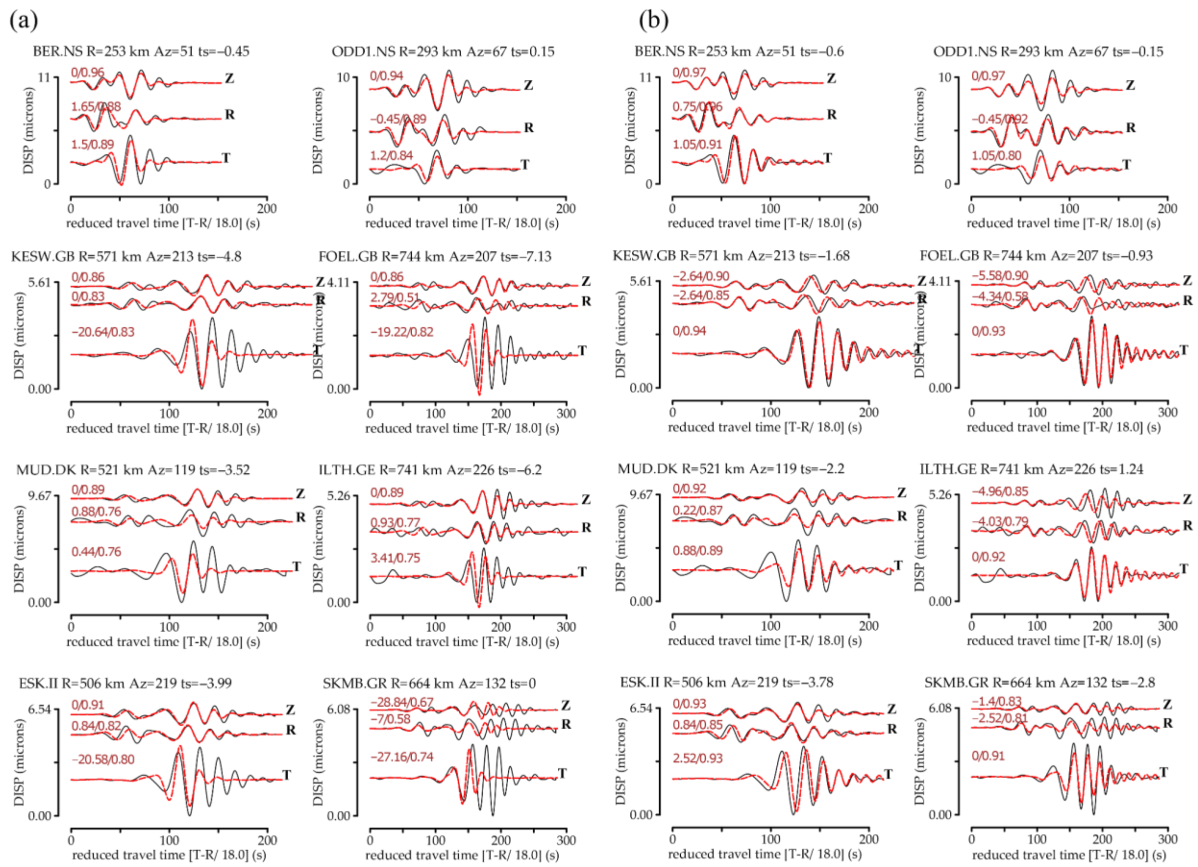


*Figure 5: Example of waveform fit comparison between the moment tensor results using Crust1.0 (a) without sediment, and (b) with sediment. The displacement observed waveforms (black lines) and synthetic waveforms (red lines) are plotted for three components (Z: vertical, R: Radial, and T: Transverse components). The station and network codes are written on the top of each trace along with hypocentral distances (R), azimuth (Az), and time shift for each station (ts). The unit of the traces are in [μm]. On the upper left of each trace, the individual trace time shift and the cross-correlation coefficient are shown respectively.*

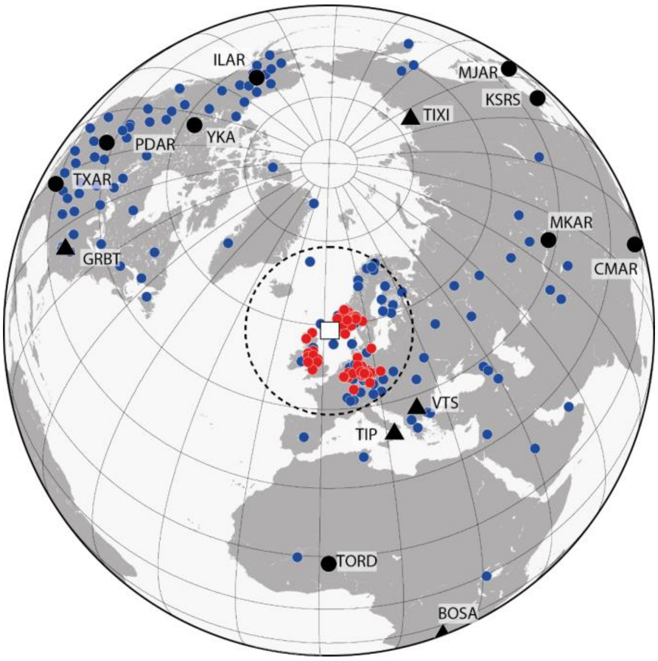


*Figure 6: Observations from the 30 June 2017 event. The blue dots mark selected stations with P-phase readings, and red dots mark stations with both P- and S-readings. Black symbols indicate seismic arrays (circles) and 3-component stations (triangles) with particularly clear depth phases. The dashed circle marks 15° of the epicenter (white square).*

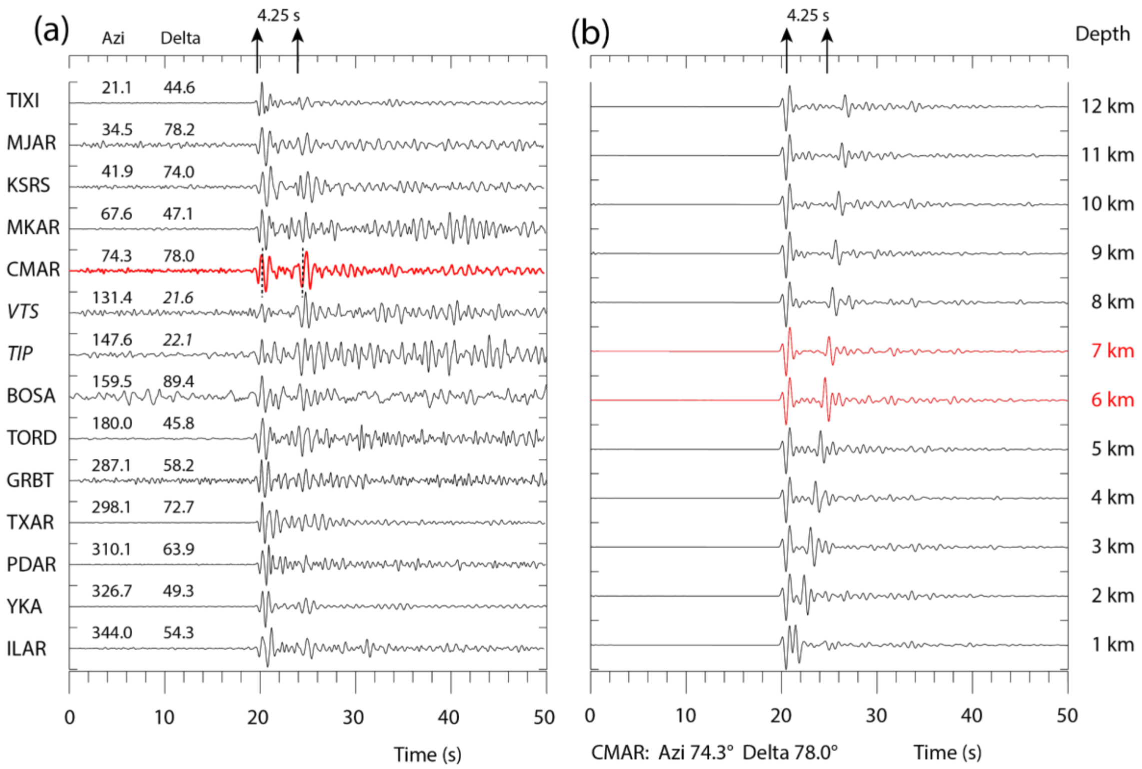


*Figure 7: a) Observations of P and depth phases from the 30 June 2017 event at teleseismic distances, sorted by azimuth. The locations of the different stations shown in this panel are shown by black symbols in Figure 6.* The vertical arrows indicate the first P-phase and the depth phase. The time-aligned traces show a relatively consistent time difference of 4.25 seconds between the two phases at all stations. *The signal from CMAR (Chiang Mai array, Thailand) holds clear P and depth phase arrivals, and is shown as the red seismogram. The data is filtered between 1.5 and 3.5 Hz. b) Waveform modelling at CMAR at different source depths. The best fit between the observed and synthetic data was at 6-7 km, indicated by the red seismograms. The data is filtered between 1 and 3 Hz.*

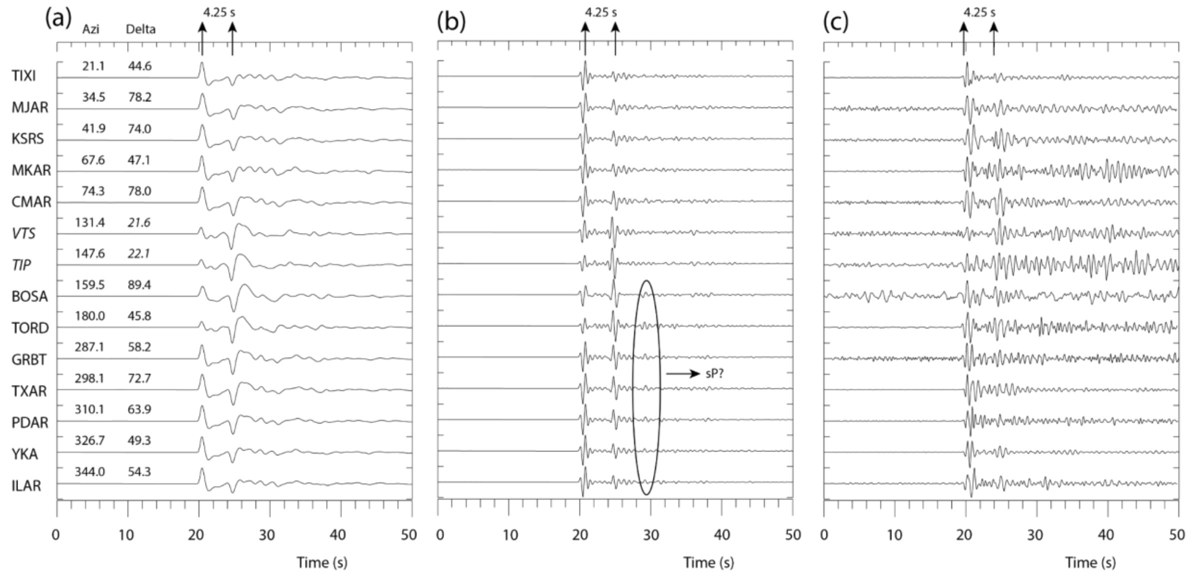


*Figure 8: a) Waveform modelling at teleseismic stations using a source at 6.5 km depth (unfiltered). b) Waveform modelling of at teleseismic stations using a source at 6.5 km depth (filtered 1-3 Hz). c) Observations at teleseismic distance (filtered 1.5-3.5 Hz). All the modelling is performed using the hudson96 algorithm.*

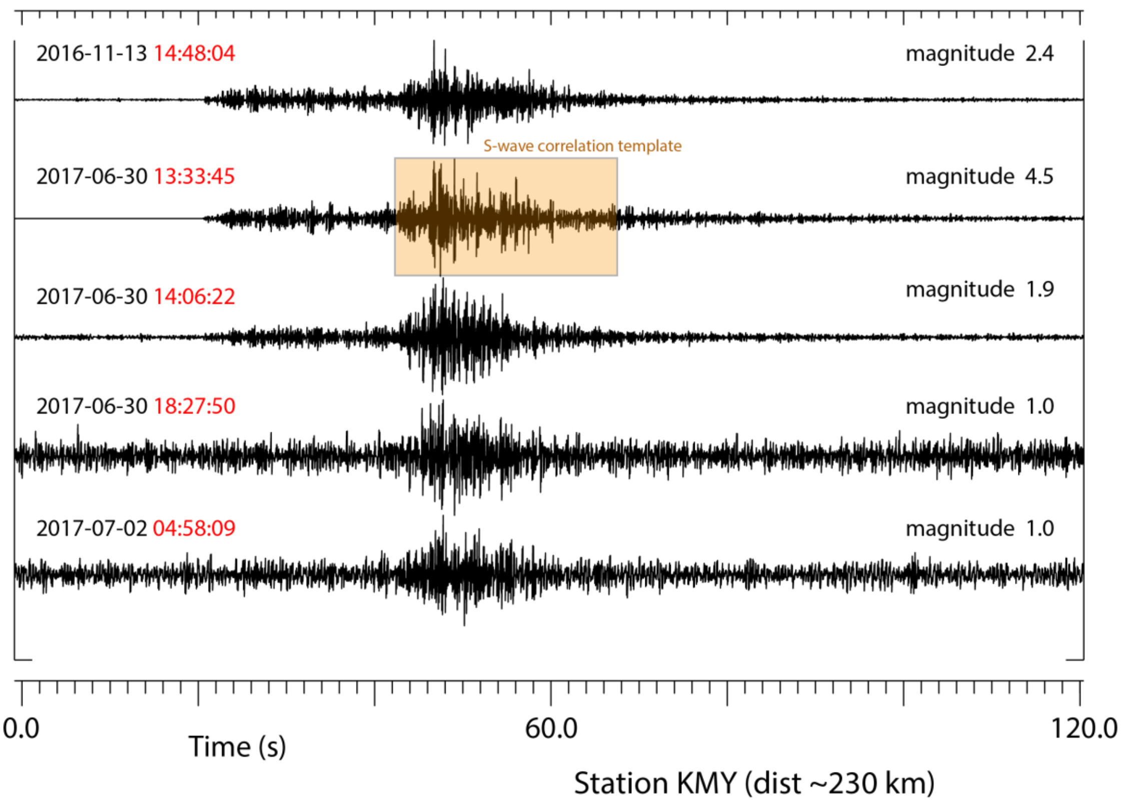

*Figure 9: Seismic events found by waveform correlation to be related to the 30 June 2017 event recorded on the NNSN station KMY at a distance of 200 km from the epicenter. All events were found using a 42-channel correlation detector on the NORSAR-array (distance 550 km) using the S-wave train from the main event as a signal template. The waveforms are filtered in a 2-5 Hz frequency band.*

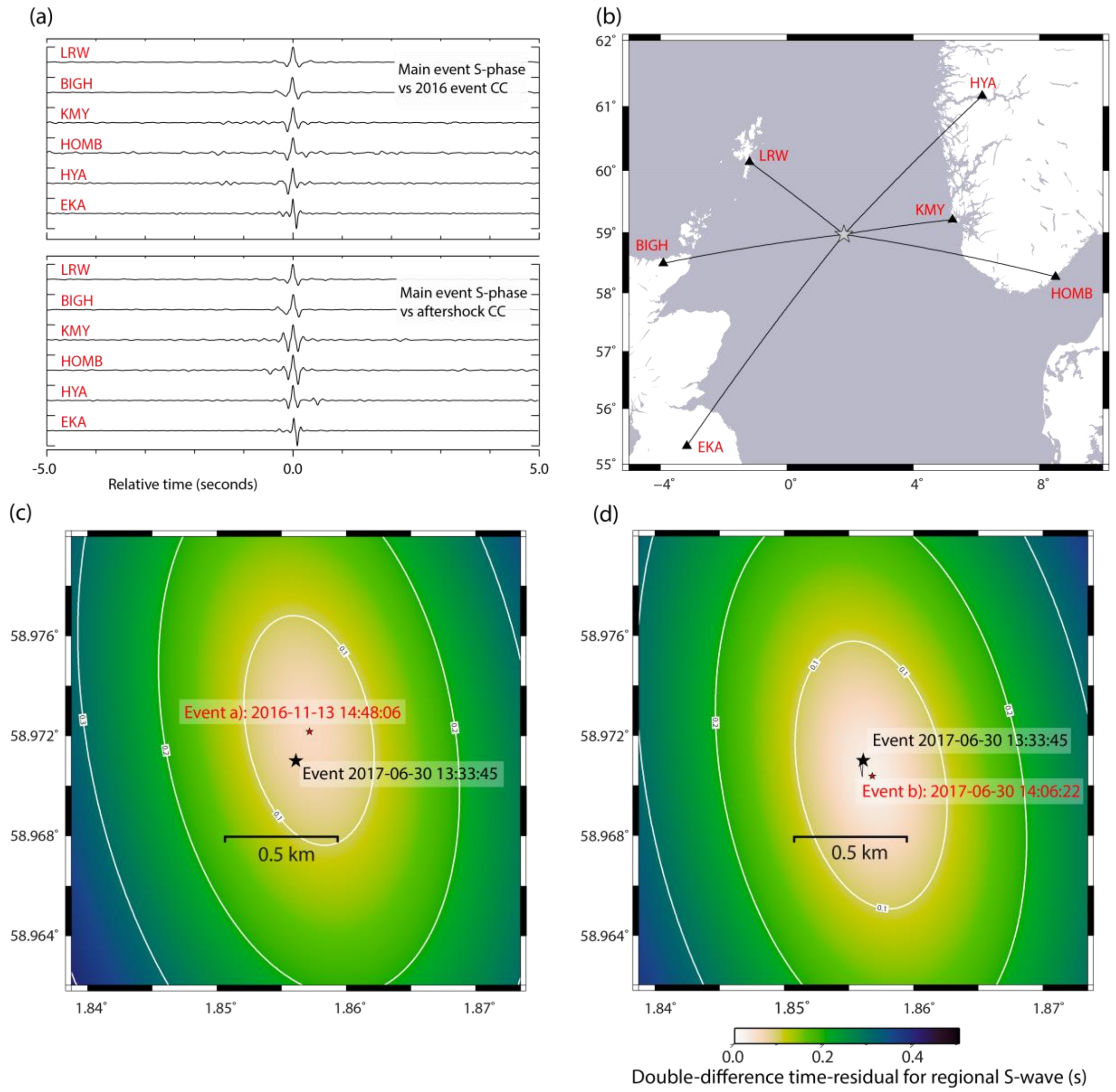

*Figure 10: Location relative to the 30 June 2017 main event (Event 2017-06-30 13:33:45) for the 13 November 2016 earthquake (panel c) and the largest aftershock on 30 June 2017 (panel d). All relative time-delay measurements were made using templates covering the S-wave arrival and coda. Panel (a) shows the correlation detection statistic traces for two events on the stations indicated in the map (b). The double-difference time-residual grids are displayed for the two events in panels (c) and (d).*

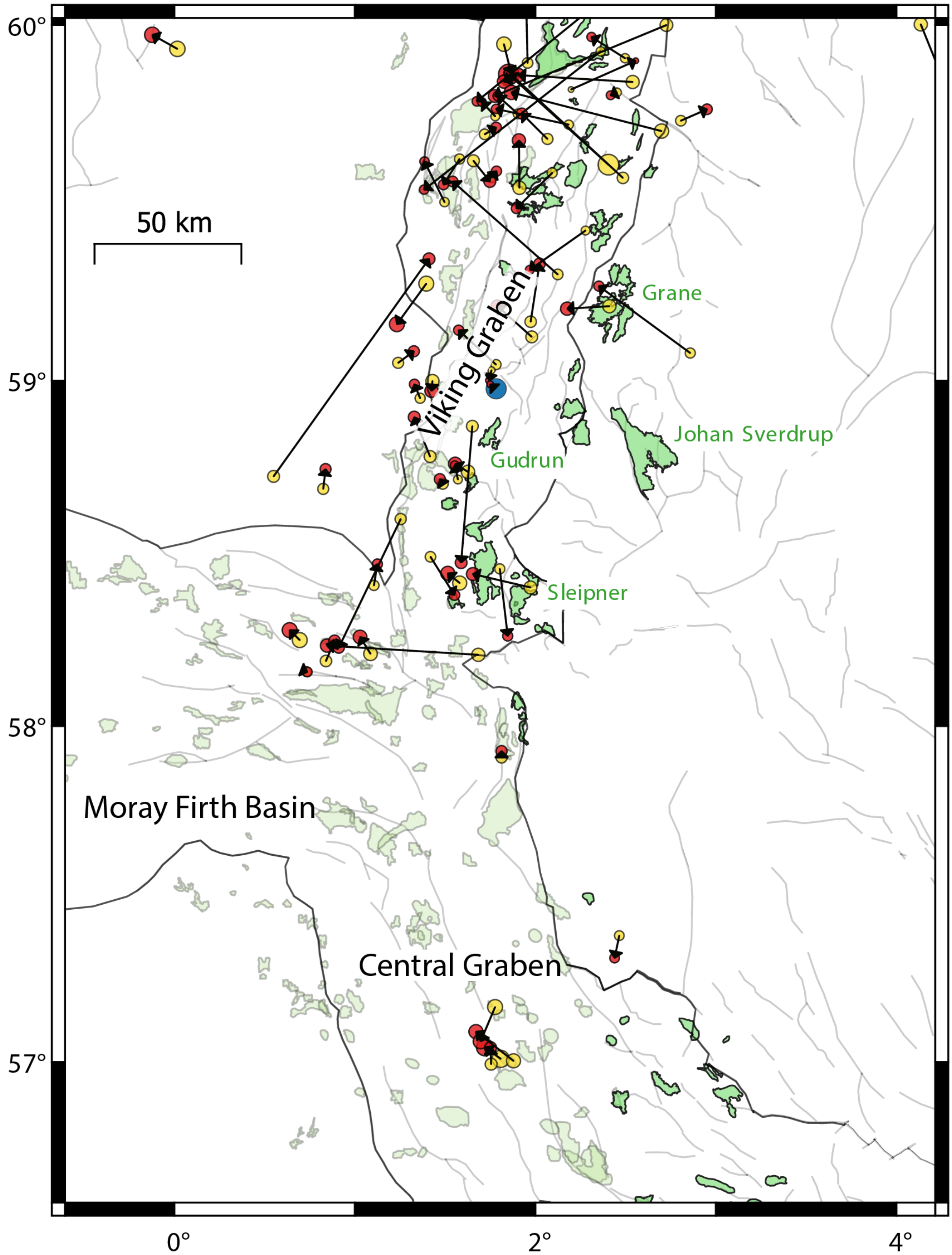

60°
59°
58°
57°
0°
2°
4°
50 km
Viking Graben
Grane
Johan Sverdrup
Gudrun
Sleipner
Moray Firth Basin
Central Graben


943

*Figure 11: Selected events from the NNSN bulletin in the period 2000-2018 (yellow symbols) and their relocations using the Bayesloc probabilistic multiple event location algorithm (red symbols). The major faults of the North Sea area are shown with grey lines and the major structures of the Mesozoic rift system are shown with black lines. Bayesloc generates joint probability distributions both for event hypocenters and for correction terms for travel time predictions. The largest relocation vectors (the longest lines) can in most cases be associated with timing errors on one or more stations. The clear green regions indicate the extent of North Sea production fields as indicated by the Norwegian Petroleum Directorate, while the lighter green regions are the production fields as given by the British Oil and Gas Authority. The location of the 30 June 2017 event is shown by the blue symbol.*